Acta Biomaterialia 193 (2025) 623–631

Contents lists available at ScienceDirect

Acta Biomaterialia

journal homepage: www.elsevier.com/locate/actbio

Full length article

Physical exercise impacts bone remodeling around bio-resorbable magnesium implants

Irene Rodriguez-Fernandez [a,b,1], Thomas Bretschneider [c,1], Andreas Menzel [a], Omer Suljevic [d], Nicole G. Sommer [d], Annelie-M. Weinberg [d], Christian Appel [a], Marianne Liebi [a,e], Ana Diaz [a], Lukas Pircher [f], Christian Hellmich [f], Uwe Y. Schwarze [d,g], Helga C. Lichtenegger [c,*], Tilman A. Grünewald [h,*]

[a] Center for Photon Science, Paul Scherrer Insitute (PSI), 5232 Villigen-PSI, Switzerland
[b] Institute for Biomedical Engineering, ETH Zürich, 8092 Zürich, Switzerland
[c] Institute of Physics and Materials Science, BOKU University, 1190 Vienna, Austria
[d] Department of Orthopedics and Traumatology, Medical University of Graz, 8036 Graz, Austria
[e] Institute of Materials, Ecole Polytechnique Federale de Lausanne (EPFL), 1015 Lausanne, Switzerland
[f] Institute for Mechanics of Materials and Structures, TU Wien, 1040 Vienna, Austria
[g] Department of Dental Medicine and Oral Health, Medical University of Graz, 8010 Graz, Austria
[h] Aix-Marseille Univ, CNRS, Centrale Med, Institut Fresnel, 13013 Marseille, France

ARTICLE INFO

Keywords:
Bioresorbable implant
Bone
Physical exercise
SAXS tensor tomography
X-ray scattering
Rat femur

ABSTRACT

Physical exercise has been shown to induce positive reactions in bone healing but next to nothing is known about how it affects the nanostructure, in particular around implants. In this study, we established this link by using small-angle X-ray scattering tensor tomography (SASTT) to investigate nanostructural parameters in 3D such as mineral particle orientation and thickness. As a model system, rat femoral bone with a bio-resorbable implant (ultra-high purity magnesium) was used. One-half of the rats underwent treadmill exercise while the other half were moving freely in a cage. At two- and six-weeks post-surgery, rats were sacrificed, and samples were taken. Our results point to an earlier start and stronger remodeling when physical exercise is applied and to a stronger reorientation of the mineralized collagen fibers around the implant. This study reveals the nanostructural response of bone with bio-resorbable implants to physical exercise. Understanding this response is very important for designing post-surgery treatments.

Statement of Significance: Physical exercise is known to have beneficial effects on the human body and is often incorporated into the recovery process following orthopedic surgeries. While the response of bone to physical exercise is well-documented, the structural response of bone to early exercise after implant placement, particularly its impact on the nanostructure, has not been extensively studied. In this study, we identify the effects of physical exercise on the bone nanostructure and the remodeling process around a bioresorbable implant. These findings could help develop tailored physical exercise strategies for post-surgery recovery in patients.

1. Introduction

Bone fractures reduce the mechanical stability of bones and can jeopardize the structural integrity of the musculoskeletal system. Orthopedic implants are often necessary to stabilize the fractured bone during the healing process but both fractures and implants completely disrupt the pre-existing load distribution in the bone. After an injury, the bone will try to adjust to the new loading pattern. The quality of the healing bone depends on its ability to remodel and adapt to the new mechanical environment. This remodeling process is governed by mechanotransduction whereby cells (osteocytes) convert mechanical signals into biochemical, electrical, or chemical responses [1–3] which induce osteoblast and osteoclast activity and differentiation of mesenchymal stem cells [4,5]. Controlled physical exercise can be used to

---

* Corresponding authors.
E-mail addresses: helga.lichtenegger@boku.ac.at (H.C. Lichtenegger), tilman.grunewald@fresnel.fr (T.A. Grünewald).

[1] These authors contributed equally

https://doi.org/10.1016/j.actbio.2024.12.008
Received 17 June 2024; Received in revised form 11 November 2024; Accepted 2 December 2024

create and moderate mechanical cues in the bone. There are prior studies on rat models without fractures or implants that focused on the macro- and microscopic effects of exercise from a medical perspective [6,7]. Positive effects were reported for parameters like bone mineral density and bone mass [8]. Exercise has been shown to improve the healing of non-critical-sized bone defects, suggesting a positive effect both of preemptive [9] and post-operative exercise [10]. Bourzac et al. also reported increased osteogenesis and elevated osteoblast activity [9].

Bio-resorbable implants are gaining increasing attention due to their possible advantages over conventional titanium (Ti) implants in orthopedics [11]. For load-bearing applications, such as fracture fixation, magnesium-based alloys seem very promising, and their biocompatibility and general suitability have already been demonstrated in the literature [12–14]. Some insights have been gathered about the response of bone structure to the placement of such implants [15–17]. However, no information exists about how physical exercise might influence the bone structure in the vicinity of a magnesium implant during the healing process. In particular, the continuous degradation of such implants causes a locally evolving situation with a continuously changing bone-implant interface and changing mechanical load patterns.

Bone has a complex hierarchical structure over multiple length scales all of which contribute to its mechanical properties and performance [18–21]. At the nanostructural level, bone is composed of mineralized collagen fibers. Some of their characteristics such as the fiber orientation or the degree of mineralization highly influence bone's mechanical properties [22] and details on the actual arrangement of the mineral fraction are still emerging [23–28]. Further insights into the nanostructural behavior are therefore essential for modeling and predicting bone healing in the future.

Traditional methods to study the bone structure, such as histology or computed tomography, do not give access to the bone nanostructure. In contrast, X-ray scattering methods provide a unique tool to characterize bone at this length scale [29–31]. In previous studies, these methods were used to show that the placement of an implant made from titanium (Ti) [32], zirconium (Zr) [33], or magnesium (Mg) [17] changed the preferential orientation of the mineral-collagen composite and thickness of the mineral particles in this composite at the bone-implant interface. A study using 2D small-angle and wide-angle X-ray scattering (SAXS, WAXS, resp.) showed changes in the bone nanostructure already one month after the implantation of an Mg implant: instead of aligning with the bone's usual direction along its main axis, mineral particles reorganized to follow the implant surface [15,16].

2D scattering methods, however, are limited to flat samples and are, thus, very dependent on sample orientation and preparation. To overcome this, 3D scattering methods such as SAXS tensor tomography (SASTT) were developed. With SASTT, 3D orientations of the nanostructure of 3D samples can be studied [34,35]. The technique was used, for instance, to report on reorientations of the bone nanostructure around the surface of a Mg-implant [36].

However, the impact of physical exercise on the bone nanostructure around Mg-implants, and – to the best of our knowledge - around implants in general, has not been studied.

Therefore, in the present work, we used SASTT and 2D SAXS techniques to determine the effects of early physical exercise applied shortly after implantation on the bone nanostructure around bio-resorbable implants during healing. We investigated bone samples from rats with a bio-resorbable implant that had been subjected to a treadmill exercise regime and were explanted 2 weeks and 6 weeks after the surgery. The results of the exercised samples are compared to non-exercised equivalent samples. We find distinct differences in nanostructural parameters such as degree of orientation of the mineral-collagen composite, direction of orientation, and mineral particle thickness in the exercised samples, suggesting a pronounced impact of early exercise.

2. Materials and methods

2.1. Samples

All animal experiments for this study were approved by the Austrian Federal Ministry for Science and Research under the following permit: BMWFW-2020-0.363.120. The animal experiments were carried out in accordance with the "European Convention for the protection of vertebrate animals used for experimental and other scientific purposes".

Male Sprague Dawley rats were randomly divided into two experimental groups, non-exercised (nEx) and exercised (Ex). At 6 weeks of age, all the rats underwent surgery as described in Suljevic et al. 2023 [10]: "After cleaning the surgical field with alcohol, transverse skin incision was made on both femur diaphysis. A cylindrical hole was then created by using a surgical drill with 1.55 mm bur at the femur diaphysis. XHP-Mg pins were implanted in a transcortical fashion by using the needle holder. The skin was closed with absorbable sutures. To ensure post-operative analgesia, all rats subcutaneously received 200 mg/kg Caprofen (Rimadyl, Pfizer Corporation, Vienna, Austria). Post-operatively, the rats were permitted to move unrestrainedly in their cages and with unrestricted weight bearing. The rat's behavior was monitored each day until the end of the experiment." More details can be found in the reference and more information about the implant is given by Okutan et al. [37]. After the implantation procedure, µCT measurements were performed. Starting on the second day after implantation, rats from the Ex-group underwent a 2-week (5 days per week) running exercise on a treadmill machine, as described in Suljevic et al. In this paper, it was shown that this protocol yields positive effects for bone regeneration and induces osteogenesis [10]. Animals were euthanized at 2 and 6 weeks after implantation.

Explanted bones were fixed, dehydrated, and embedded in PMMA, Technovit 9100 New (Heraeus Kulzer, Wehrheim, Germany) as described in Suljevic et al. [10]. Two groups of samples were cut/machined using a precision saw "Struers Accutom 50″ (Struers, Ballerup, Denmark). 1) Small cylinders (5–7 mm length, 3 mm diameter) which contained the implant plus surrounding bone, with the longitudinal implant axis and the cylinder axis co-aligned for SASTT measurements. Four samples were prepared, one for each time point and exercise condition: 2w-nEx (2-week non-exercised), 2w-Ex (2-week exercised), 6w-nEx (6-week non-exercised), and 6w-Ex (6-week exercised). Each sample came from a different animal. 2) Thin slices (200 µm thickness) of bone with implant which were cut in a plane containing longitudinal bone and implant axes for SAXS measurements. Three samples of different animals were prepared for each time point and exercise condition except for 2w-nEx where only 2 samples were possible to obtain due to sample preparation problems with one sample. All samples correspond to the left leg of the animal except the SASTT 2w-nEx and two of the SAXS 2w-Ex where the right leg was used due to problems with the left-leg samples.

2.2. MicroCT

In vivo micro-computed tomography (µCT) of femoral bones was performed using a Bruker Skyscan (Bruker Skyscan, Kontich, Belgium) directly after surgery. During the µCT rats were positioned on their back with femur bones oriented at a 90° angle. The image reconstruction was performed using NRecon software (Skyscan, Kontich, Belgium). Relevant parameters for measurements and reconstructions are provided in Supplementary Table S2.

2.3. Small-angle X-ray scattering

Small-angle X-ray scattering (SAXS) experiments were performed at the cSAXS beamline of the Swiss Light Source (SLS) at the Paul Scherrer Institute, Villigen, Switzerland, using a monochromatic beam of 12.4 keV. The beam was focused to a beamsize of 25×20 µm^2. To minimize air scattering, an evacuated flight tube was placed between the sample and the Pilatus 2M detector. The sample-detector distance was 2.18 m, which covers a q-range of 0.1–5 nm^{-1}, where q is the scattering vector $q = 4\pi/\lambda \sin(\theta)$, where λ is the wavelength and θ the half scattering angle. The direct beam intensity was measured using light scattered from a 1.5 mm steel beamstop inside the flight tube. The samples were mounted on a motorized stage with X-Y movement and scanned with a step size of 20 µm in both directions, with fly scans in the Y-direction and an exposure time of 30 ms.

2.4. SAXS tensor tomography

SAXS tensor tomography (SASTT) experiments were also performed at the cSAXS beamline with a monochromatic beam of 17.8 keV focused to approximately 60 × 30 µm^2. Other details from the setup are similar to the small-angle X-ray scattering experiments described above. The cylindrical samples were mounted on a needle and placed on a two-axis goniometer which allows for tilt δ, rotation γ, and translation in the X-Y plane to scan the samples. More details about the SASTT setup can be found in Liebi et al. [34]. The samples were scanned with a step size of 65 µm and an exposure time of 30 ms. Between 298 and 338 projections were acquired for each sample. Projections were captured at 7 different tilt angles (δ), equally distributed between 0 and 45° For $\delta = 0°$, the rotation angle γ was varied from 0° to 180° For all other tile angles, γ ranged from 0° to 360° For more details about the specific experimental parameters with which each sample was measured see Supplementary Table S1. The small differences in experimental parameters between samples are not significant enough to affect the SASTT results.

The total dose of the experiments was estimated as described by Silva Barreto [38] following Eq. (1):

$$Dose = \frac{E\ I_o \tau\ A}{\Delta x \Delta y \Delta z\ \rho} N \tag{1}$$

where E is the X-ray energy, I_0 the photon flux, τ the exposure time, A the absorption of the sample, $\Delta x \Delta y \Delta z$ the sample volume, ρ the density of the sample, and N the number of projections.

The total dose of the measurements was 55 kGy for each sample. In between changes of tilt angle, and extra projection at $\delta = 0°$ and $\gamma = 0°$ was acquired to inspect changes due to radiation damage and no noticeable changes were observed in the mineral component of the bone.

2.5. SASTT data analysis

All the data, including the 2D SAXS measurements was integrated azimuthally in 16 segments using the cSAXS MATLAB package [39].

For SASTT reconstructions, the scattering signal of the mineral particles was analyzed for $q = 0.407$–0.698 nm^{-1}. All the projections were aligned using an iterative method [40] and the reconstruction was performed as described in Liebi et al. [41]. The 3D reciprocal space map in each voxel is described by spherical harmonics with coefficients a_m^l, with orders $m = [0,0,0,0]$ and degrees $l = [0,2,4,6]$ and the orientation parameterized with the spherical angles θ and φ.

From the reconstructed 3D reciprocal space map, the main orientation and the degree of orientation were obtained. The degree of orientation is calculated as defined in Liebi et al. [41].

2.5.1. Mineral particle dimensions

To estimate the mineral particle thickness, a q-resolved reconstruction was performed. The q vector was divided into 175 logarithmically spaced segments in the q-range [0.04–5.6 nm^{-1}] and a reconstruction of the symmetric scattering intensity was performed for each one of them, i.e., a reconstruction by optimizing the first coefficient ($m = 0$, $l = 0$).

The T-parameter was calculated using the stack-of-cards model [42], which models the mineral platelets as randomly spaced, parallel stacked particles. The T-parameter can be obtained from Eq. (2), where P is the Porod constant (extracted from the Porod plot Iq^4 vs q^4) and $G(x)$ is a rescaled function described in Eq. (3) and $x = qT$. In Eq. (3), α denotes the damping of the oscillations and β represents the spatial correlation between particles.

$$q^2 I(q) = \frac{\pi}{4} P T^2 G(x) \tag{2}$$

$$G(x) = \frac{4}{\pi} \frac{x^2 + (\alpha - 1)(\alpha^2 + \beta^2)}{(x^2 + \alpha^2 - \beta^2)^2 + 4\alpha^2\beta^2} \tag{3}$$

This model assumes a two-phase system with sharp interfaces, platelet-shaped particles, and a mineral volume fraction of 50 % [43].

The Guinier exponent (R) is calculated with a power-law fit in the Guinier region, following Eq. (4). The T-parameter was then calculated for each pixel where $R < 2$ to comply with the boundary conditions of the T-parameter analysis, along with a symmetric intensity threshold of 2 to eliminate signals that have not originated from bone.

$$I(q) = aq^{-R} \tag{4}$$

2.6. Further processing of tomography data

Previous studies showed that some nanostructural parameters vary with the distance to the implant [15,32,36]. The following steps were taken to enable and simplify this distance-resolved analysis. Samples were carefully machined and later, during the measurement, positioned so that the implant axis was parallel to the Y-axis of the experimental setup (see Fig. 1 for coordinate system). From the SASTT absorption tomogram, a virtual slice in the X-Z plane was extracted at each end of the implant. First, an edge-finding algorithm was used to detect the interface between the implant and surrounding material. Then, a circle-finding algorithm was used to fit a circle into the results of the edge finding and extract the center coordinates. Using the center coordinates at both sides of the implant, a linear function was constructed, and implant center coordinates were extrapolated for each X-Z slice. Afterward, the distance to the implant center was calculated for each voxel within the respective X-Z slice. The implants were manufactured with a diameter of 1.6 mm and the bone samples were machined into cylinders with a diameter of approximately 3 mm. According to these specifications, voxels with a distance to the implant center between 0.8–1.5 mm were considered for the distance-to-implant analysis. This dataset was grouped into ten distance ranges, each covering 70 µm radially. The median value of each parameter of interest was calculated for each distance group and plotted at the mean distance of the group respectively.

2.6.1. Segmentation

We distinguished between bone that had been present right after the implantation (previously existing) and bone that formed during the recovery period (newly formed). For this purpose, we used in vivo micro-CT measurements, performed shortly after the implantation surgery (as described in Section 2.2), and the SASTT measurements, performed on the explanted samples. If bone was present in the same location in both measurements, then this area was labeled as previously existing bone. Alternatively, if bone was present only in SASTT but not in the µCT dataset, it was labeled as newly formed bone, as it must have formed between implantation and sacrifice. To determine if bone is present in the same location, we spatially correlated the voxels of the two datasets. First, both datasets of the same sample were aligned by visually matching morphological characteristics using Paraview software (http://www.paraview.org). Every subsequent step was performed with self-written Python scripts.

The coordinates of the µCT dataset were transformed in order to place the aligned tomograms in one coordinate system. It must be considered that the volume of a voxel from one dataset could correspond

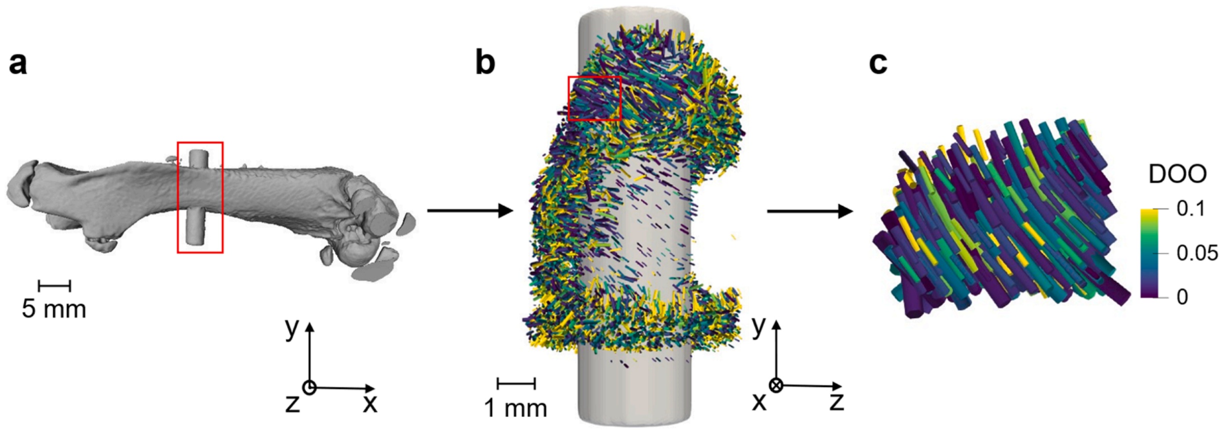

Fig. 1. Experimental procedure. (a) In vivo μCT reconstruction of the femur with implant. The red square delimits the part that was extracted and measured with SASTT. (b) SASTT reconstruction of the implant (grey) with the surrounding bone. The glyphs represent the main orientation of the mineralized collagen fibers in each voxel (direction), scattering intensity (size) and degree of orientation (color). (c) Extracted subvolume of SASTT reconstruction, area delimited by red square in b).

to multiple voxels of the other dataset. In our approach, a μCT voxel was assigned to the SASTT voxel that held most of its volume fraction. Since the μCT was performed with a smaller voxel size (40 μm) than SASTT (65 μm), every SASTT voxel was correlated with one or more μCT voxels. In the case that the correlation was done with multiple μCT voxels these were only labeled as bone if >50 % of the corresponding voxels were considered bone. A SASTT voxel was considered bone if it fulfilled the requirements described in Section 2.5.1 whereas voxels in the μCT were considered bone if the grey level of the voxel was higher than a threshold of 120.

2.6.2. Statistics

Statistical analysis was performed for SASTT data comparing consecutive distance steps using one-way analysis of variance (ANOVA), which is a statistical method that allows us to compare multiple groups (in this case, distance steps) at once to determine if there are significant differences between them. Specifically, ANOVA compares the variation within each group to the variation between groups. If the differences between groups are greater than the differences within groups, this signals that there is a meaningful difference in at least one of the groups.

After ANOVA identified an overall difference, we conducted a post hoc Bonferroni test to pinpoint where those differences lie. The Bonferroni test adjusts the significance level to account for the increased risk of finding differences purely by chance due to the number of comparisons being made. By reducing the chance of false positives, it ensures that we only consider a difference significant if there is strong enough evidence that the difference is not due to random variation.

Significant differences were identified using a *p*-value threshold of 0.05, meaning that if the probability of observing a difference as large as the one seen (or larger) purely by chance is <5 %, the difference is considered statistically significant. These significant differences were marked in the respective figures to help visualize which distance steps were meaningfully different from one another.

The results of the statistical analysis are presented in Supplementary Figure S1.

2.6.3. Standard error of mean

The standard error of the mean was calculated for each sample at each distance step, and it includes every voxel located at each distance step (i.e., a few thousand voxels). We furthermore want to point out that the nanoscale information presented is an average over the whole voxel volume.

3. Results

To investigate the effects of physical exercise on bone remodeling around Mg implants, rat femur samples with an implanted Mg-pin were studied at different time points and after an exercise regime had been applied. The rats were divided into two groups: those who underwent a running exercise (Ex) and those who were moving freely in a cage (nEx) (see Section 2.1 for details). The animals were euthanized 2 and 6 weeks after the implantation surgery (2 w and 6 w).

Once the femurs were explanted, the samples were prepared including the implant and surrounding bone, covering the area delimited by the red square in Fig. 1a. One sample of each group was measured with SAXS tensor tomography (SASTT). This allowed us to obtain in each voxel of a three-dimensional sample the three-dimensional orientation of the mineralized collagen fibers and the degree of orientation. Fig. 1b shows a SASTT reconstruction of one of the samples, with an extracted magnified subvolume in Fig. 1c. In the SASTT reconstructions, the direction of the glyphs represents the preferred orientation of the fibers, the glyph size scales with the scattering intensity, and the color represents the degree of orientation (DOO).

To add statistics and study larger fields of view, 2D SAXS measurements were performed. (Supplementary Figures S2-S3).

In the acquired 3D data, we observed endosteal and periosteal callus formation after implantation. For this reason, we segmented the data into previously existing bone and newly formed bone to study the effect of physical exercise and the implant in these two regions. Fig. 2a shows the segmented bone volume for the 6w-Ex sample, the other samples can be found in Supplementary Figure S4. This segmentation was performed as described in the methods section (Section 2.6.1). Bone that had been present at the time of implantation was labeled as previously existing bone (Fig. 2b-d) whereas bone that had not been present, i.e., appeared after implantation as a response to the fracture and the implant, was labeled as newly formed bone (Fig. 2e-g). Since bone remodels constantly, the term ‘previously existing bone’ designates the spatial area where bone was present right after the implantation, not that bone within this area stayed unaltered.

3.1. Degree of orientation

In scattering experiments, the anisotropy of the mineral-collagen composite can be evaluated by the degree of orientation (DOO) [44]. This parameter is defined as the ratio between the anisotropic scattering and the total scattering, which gives an indication of how much fibers are aligned to each other in each voxel.

Fig. 2 (c,f) illustrates the degree of orientation for each sample as a

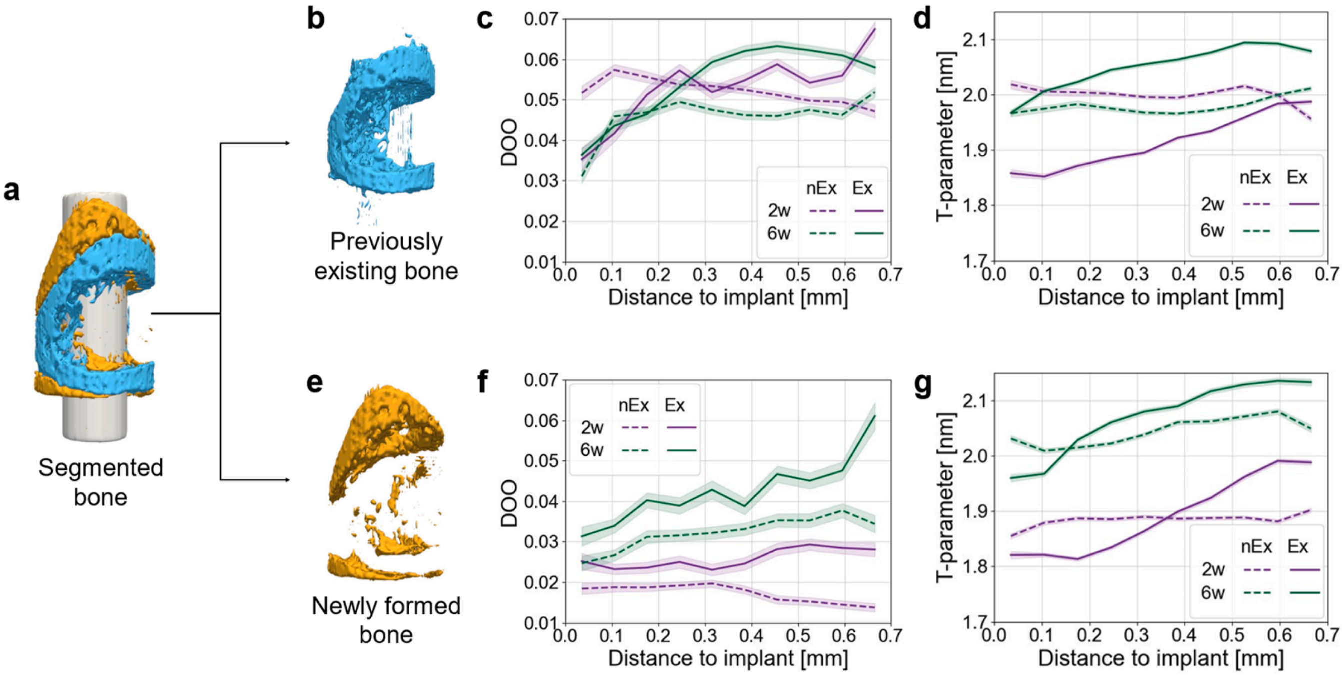

Fig. 2. Segmented bone nanostructural properties. (a) Segmentation of previously existing and newly formed bone of 6w-Ex sample. Separated volumes of previously existing bone (b) and newly formed bone (e). Degree of orientation (DOO) as a function of distance to the implant interface for previously existing bone (c) and newly formed bone (f). *T*-parameter as a function of distance to the implant interface for previously existing bone (d) and newly formed bone (g). Each sample is represented by a curve and labeled by their time point of extraction (2 weeks or 6 weeks) and the physical exercise regime (non-exercised (nEx) or exercised (Ex)). The shaded regions represent the standard error of the mean. The line plots (c-d, f-g) with statistical analysis to mark significant differences between consecutive distance steps can be found in Supplementary Fig. S1.

function of the distance from the bone-implant interface. The data is averaged over all voxels in the sample falling within a specific distance range as explained in the methods section (Section 2.6).

In previously existing bone (Fig. 2c), all samples, except 2 weeks non-exercised (2w-nEx), show a steep increase and comparable values within the first 300 µm from the implant. Farther from the implant, samples that underwent physical exercise exhibit higher DOO values than their non-exercised counterparts. In the newly formed bone regions (Fig. 2c), we observed a more constant increase of the DOO towards greater distances. While there is a generally higher DOO in previously existing bone regions compared to newly formed bone, exercised samples exhibit higher DOO values than their non-exercised equivalents in both bone regions. In the newly formed bone region, there is also a difference between the two time points, with the 6 weeks samples exhibiting generally higher DOO than the 2 weeks samples.

3.2. Mineral particle thickness

In Fig. 2 (d,g), the *T*-parameter, an indicator of the thickness of mineral particles [29], for each sample is presented as a function of the distance from the bone-implant interface.

In both previously existing bone (Fig. 2d) and newly formed bone (Fig. 2g) regions, we see a rather constant value of the *T*-parameter in the non-exercised samples while the exercised samples exhibit an increase towards higher distances. In general, the *T*-parameter at 6 weeks (6 w) is notably higher in the exercised sample in both bone regions. Also, the time point seemed to play a role, with the 2-week samples showing generally lower *T*-parameters than the 6-week samples, except for previously existing bone region of the 2w-nEx sample.

3.3. Orientation of the mineral-collagen composite

We analyzed the main orientation in every voxel to understand changes due to implant placement and the exercise regime. In this analysis, it is assumed that the direction obtained from the SAXS of the mineral component is coaligned with the fibrillar direction of the collagen as demonstrated in previous studies [45].

Here, we are interested in knowing how much the local orientation in each voxel differs from the typical preferred orientation of the mineral-collagen composite in the shaft of long bones, i.e., the longitudinal bone axis. For this purpose, we calculated the angle between the main mineral-collagen orientation in each voxel and the longitudinal bone axis, derived from the dot product of the two vectors. In Fig. 3a this angle is plotted as a function of the distance to the bone-implant interface for areas of previously existing bone. The 2w-nEx sample shows the smallest orientation deviation from the longitudinal bone axis (X-axis) and a rather constant trend. The other three samples exhibit a more pronounced deviation from the bone axis close to the bone-implant interface. With increasing distance, the alignment becomes increasingly parallel to the bone axis and seems to approach a common baseline. The mineral-collagen composite in exercised samples shows greater deviation from the longitudinal bone axis than in the corresponding nEx samples.

These findings are also visible when looking at Fig. 3b. Here, each glyph represents the median of the orientation of the mineral-collagen composite of all voxels along the implant direction (Y-axis). The color shows the median along the Y-axis of the angle between the longitudinal bone axis (X) and the main orientation in each voxel. A dark blue glyph represents an orientation parallel to the bone axis and a red one perpendicular to it.

In Fig. 3b we see that in the previously existing bone region of the 2w-nEx sample the mineral-collagen composite is strongly oriented along the main bone axis (mostly dark blue glyphs). The same holds for the 2w-Ex samples, although slight deviations are visible. In both 6-week samples (6w-nEx and 6w-Ex), there are regions with an orientation away from the main direction of the bone axis, shown in red. These areas are located close to the implant, in proximal and distal directions. In a 3D visualization of the data (Supplementary Video S1-S4), it can be seen

Previously Existing Bone

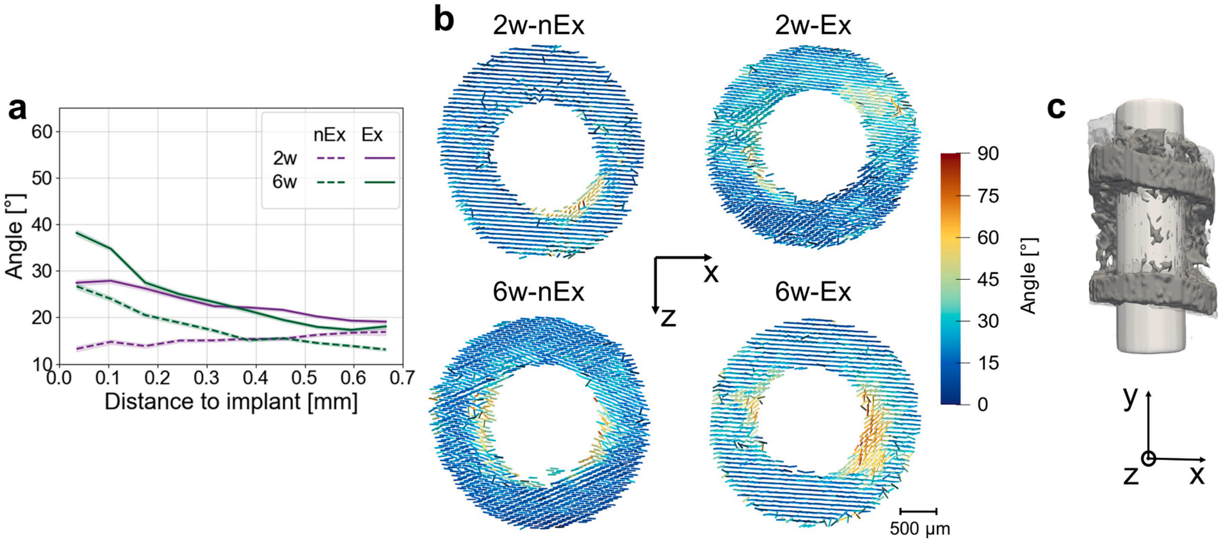

Newly Formed Bone

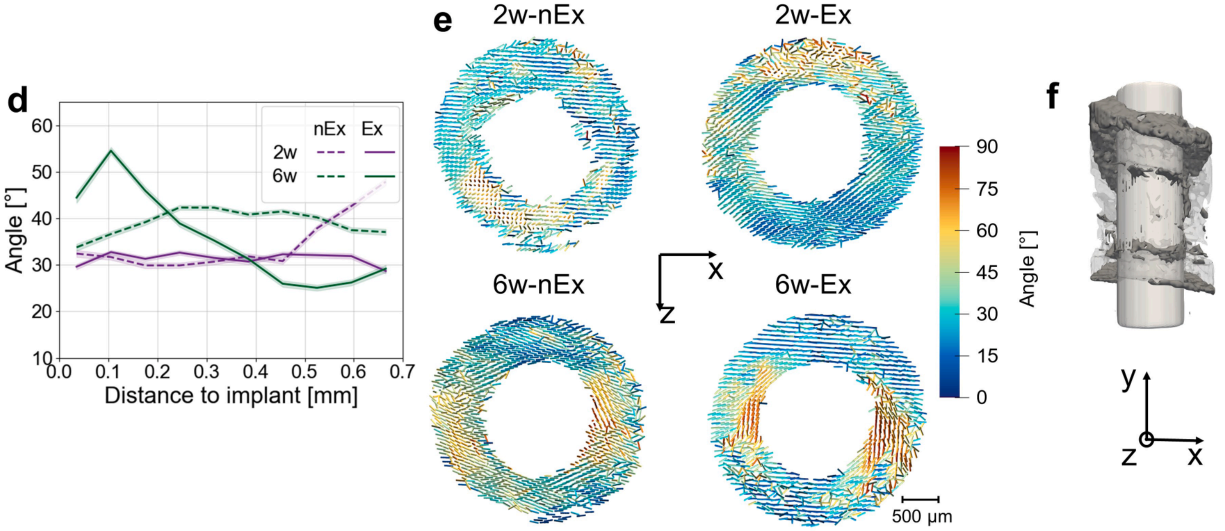

Fig. 3. Orientation results for previously existing bone (a-c) and newly formed bone (d-f). (a,d) Line plots of the angle between the longitudinal bone axis and the local orientation as a function of distance to the bone-implant interface. (b,e) Median of the orientation of the mineral-collagen composite along the implant (Y-direction). Orientations are represented by colored glyphs. The color represents the median along the Y-axis of the angle between the longitudinal bone axis (X-direction) and the main mineral-collagen composite orientation in each voxel. Glyphs are not scaled with any magnitude. (c,f) 3D visualization of the segmented sample (6w-Ex) and coordinate system as a reference. The line plots (a,d) with statistical analysis to mark significant differences between consecutive distance steps can be found in Supplementary Figure S1.

how the reorientation is forming a wrapping pattern of mineralized fibers, around the implant. This wrapping is more pronounced in the 6-week exercised sample than in the 6-week non-exercised sample.

For newly formed bone (Fig. 3d-f) the behavior is different. At 2 weeks it can be observed in Fig. 3e that there are seemingly randomly localized areas, whose orientations differ from the main bone axis, for both, Ex and nEx samples. At 6 weeks, the wrapping pattern that has been described above for the previously existing bone (Fig. 3b) is also present for both Ex and n-Ex samples. We note that the effect is considerably more pronounced in the exercised sample 6w-Ex, where strong orientation away from the longitudinal bone axis and along the implant surface was observed close to the implant (Fig 3. d-e). In general, in the newly formed bone regions, a greater amount of random orientation and a stronger wrapping effect was observed than in the previously existing bone.

The results of degree of orientation and *T*-parameter are supported by the results of 2D SAXS measurements (Supplementary Figures S2-S3). As in scanning SAXS only one plane is measured instead of a 3D full volume in SASTT, and the orientation and therewith the degree of orientation are only measured as a projection within this plane, discrepancies are expected. However, the general shape agrees for the degree of orientation which is larger at 6 weeks when compared to 2 weeks, and the DOO of the 6w-Ex sample increases far away from the implant. In the case of the *T*-parameter, 6-week samples show higher values than 2 weeks but the differences between exercised and non-exercised samples are not as clear as with SASTT. No detailed orientation analysis was done in this case, because analyzing the orientations in 2D does not allow for a meaningful comparison with the 3D orientation angles from SASTT results.

4. Discussion

4.1. Effects of physical exercise

In this study, we investigated the impact of physical exercise on the remodeling of bone around bio-resorbable implants. While exercise has been shown to have a positive impact on bone healing in terms of bone mineral density and osteogenesis [8,9], this study shows, as a major result, that physical exercise has distinct effects also on the bone nanostructure around magnesium implants. This information is essential for understanding the healing process of bone around such implants and obtaining information about the impact of mechanical stimuli. Specifically, our results show that the degree of orientation (DOO) of the mineral-collagen composite was generally higher in exercised bone, specifically at the time point of 6 weeks after implantation (Fig. 2c,f). This phenomenon is particularly pronounced in newly formed bone which could indicate enhanced healing of callus tissue whereby woven bone is remodeled into lamellar bone. This transition can also be observed in histological images of stained bone slices from samples that underwent the same protocol (Supplementary Figure S5). The morphology of the newly formed bone changes in appearance over time, transitioning from a more fibrous and immature-looking structure in the 2-week samples to a more compact structure in the 6-week samples. During early stages of bone formation, poorly ordered woven bone is laid down and slowly replaced by lamellar bone which is known to have a higher DOO, as described in Liu et al. [46]. In this paper, the authors show a biphasic mineralization process with a first wave of unorganized, woven bone tissue formation within 2–6 weeks and a second wave of transformation into organized, lamellar bone within 6–9 weeks. It has been shown in mice, that the woven bone is characterized by a lower degree of mineralization and orientation as well as slightly thicker mineral particles compared to lamellar bone [47]. We hypothesize that the training is accelerating the transformation process from woven bone to lamellar bone.

Furthermore, the mineral platelet thickness, which is an indicator of bone maturity, was smaller at the interface to the implant in the exercised samples and greater in regions further away from the implant (Fig. 2d,g) whereas it remained more constant in the non-exercised samples. Both of these results suggest that physical exercise accelerates the start and/or development of structural changes in the bone.

In mature/healthy bone, i.e., without an implant, the mineral-collagen composite tends to orient along the longitudinal bone axis in both humans [20,48], and rats [49,50]. However, it has been shown that mechanical stimuli can alter the orientation of the mineral-collagen composite [51,52]. Moreover, bone orientation often differs locally from this alignment around macrostructural features such as cement lines, blood vessels, etc., underlining the importance of studying local orientations [24,53–55]. In this study, we observed a more pronounced preferred orientation away from the bone axis in exercised rats than in non-exercised rats, which is indicative of a stronger structural adaptation of bone to the new geometry and the changed loading pattern. We also observed a more isotropic behavior close to the bone-implant interface (Fig. 3).

While our results clearly show nanostructural changes around the implant, it is in general difficult to determine the onset of nanostructural remodeling. Basic multicellular units (BMU) at the bone-implant interface were observed as early as two weeks after administration of a Ti implant [56], and altered mineralized nanostructure was confirmed as early as one month after implantation [36]. However, information regarding earlier time points is limited. Our results show that without exercise no significant amount of altered mineralized nanostructure is present after two weeks post-surgery. If physical exercise is applied, the remodeling process seems to proceed quicker and altered mineralized nanostructure is already formed after two weeks as can be seen in the degree of orientation (Fig. 2c) and orientation of the mineralized fibers (Fig. 3a).

According to our results, exercise leads to a decrease in the mineral particle thickness close to the implant and a stronger reorientation of the mineral-collagen fibers. Thinner mineral particles are associated with younger bone [29] expected during primary or early secondary mineralization in the remodeling process. While reorientation of the fibers around implants has been observed before, the impact of physical activity had not been studied. Here we show for the first time that physical exercise leads to a faster and stronger reorientation of the collagen-mineral composite around the implant in the form of a wrapping pattern. Therefore, we hypothesize that those effects on the nanostructure originate from stronger remodeling around the implant initiated by physical exercise. Enhanced remodeling in rat bone due to exercise, specifically in previously existing bone, has not been reported in literature yet, possibly because of insufficient sensitivity of common biochemical markers used to track changes in bone remodeling.

To the best of our knowledge, our study is the first one to provide insight into the effect of exercise on the nanostructure of bone around implants. Since it is well known that the nanostructure in turn influences the mechanical properties of bone, this information can become crucial to assess and potentially even predict bone quality after implant placement and subsequent exercise.

4.2. Further implant-induced effects

Prior studies on the effects of bio-resorbable and permanent implants on bone nanostructure found several features that are believed to be a direct consequence of the presence of an implant.

The mineral-collagen composite exhibited a general decrease in degree of orientation near the implant. This response is commonly observed in bone adjacent to orthopedic implants, as evidenced by 2D SAXS [16,17,32,52,57] and SASTT [36]. The most plausible explanation is that the ongoing healing/remodeling process gives rise to a locally higher ratio of early-stage woven bone, which has been shown to be more isotropic than more mature bone [58]. We did not see this effect in the 2w-nEx sample, possibly because remodeled structures are not sufficiently mineralized yet to be detected by SAXS/SASTT. However, we observed different DOO trends in previously existing and newly formed bone. In the case of previously existing bone, there is a marked decline in DOO near the implant, a pattern likely due to the remodeling predominantly occurring in this area. Conversely, the DOO trend in newly formed bone exhibits a more gradual decline, which might be attributed to a gradient in bone maturation due to successive bone deposition.

Another prominent reaction of bone to implants is a distinct reorientation of mineral particles along the implant surface in surrounding bone [16,32,36]. The consensus is that the implant surface acts as a directional guide for deposited collagen fibers, such as for bone growing in scaffolds [59,60]. Since the reorientation had also been observed further away from the implant surface, local stress distributions are believed to be an additional factor driving this reorientation.

Our results for orientation in previously existing bone show a reorientation along the implant surface, close to the implant. This reorientation occurs primarily in areas with high angles between the long bone axis and implant surface (proximal and distal directions). Areas where reorientation is less pronounced are mostly located where the angle between long bone axis and implant surface is low and less local stress is acting. This general alignment with the implant surface agrees well with reported findings in literature [16,32,36].

Only the non-exercised 2-week sample does not show much reorientation and is primarily aligned parallel to the bone axis. Again, we hypothesize that the adjustment to the implant and associated remodeling is not yet evolved enough to be detectable by SAXS/SASTT at this time after implantation.

At 2 weeks after implantation, mineral particles in newly formed bone may appear to have a random orientation, suggesting a disordered growth pattern akin to woven bone. Subsequently, at 6 weeks after implantation, the orientation of the bone seems to align with the implant, similar to the alignment observed in pre-existing bone but with a more pronounced reorientation.

An explanation for these observations could lie in the significant changes within the local mechanical environment, as bone regenerates. Initially, small sections of bone form in response to the prevailing loading patterns. As these segments undergo mineralization and stabilize, they alter the mechanical environment. This, in turn, affects the orientation of subsequent bone formation, aligning it with the new mechanical context.

It is important to note that our study also faces some limitations. First, due to the limited access to synchrotron experiments, we could only perform 3D SASTT measurements of one sample per group. An advancement in this regard will be the current advent of fourth generation synchrotrons which allows for faster measurements. In this study, we tried to mitigate this limitation by performing 2D SAXS experiments to increase the relevance of the study and confirm our 3D observations on more 2D samples. The second limitation is that our study focuses on XHP-Mg implants but the effect of physical exercise on bone might vary when exposed to different implant materials. Moreover, as highlighted by Sulvejic et al. [10], different exercise protocols may yield other results, and more protocols need to be explored to gain a comprehensive understanding of the effects. Lastly, while our study focused on the short-term effects of exercise, an expansion towards the long-term evolution of the nanostructure as the implant degrades would be desirable. This aspect will be particularly important when considering potential implications for applications in a medical setting.

All in all, our results suggest that bone remodeling around implants is highly susceptible to exercise, which not only gives insight into the interplay between mechanical stimuli and bone healing but might also influence future clinical approaches involving targeted training of patients.

5. Conclusion

The effect of physical exercise on the bone nanostructure around bioresorbable Mg implants was studied in 3D with SAXS tensor tomography and 2D SAXS. We observed significant effects of exercise on the nanostructure, which point to an earlier start of remodeling when physical exercise is applied and to a stronger remodeling from woven to cortical bone. The remodeling was characterized by a reorientation of the mineralized collagen fibers around the implant.

This study provides insight into bone's nanostructural behavior around Mg implants and its response to physical exercise. Although more research is needed, our results may eventually contribute to optimizing the recovery process of patients after the insertion of an orthopedic implant with a more active approach towards rehabilitation. The results of this study will also contribute to predicting bone quality and mechanical performance in the presence of (bio-resorbable) implants.

CRediT authorship contribution statement

Irene Rodriguez-Fernandez: Conceptualization, Data curation, Formal analysis, Investigation, Software, Visualization, Writing – original draft. **Thomas Bretschneider:** Conceptualization, Data curation, Formal analysis, Investigation, Software, Visualization, Writing – original draft. **Andreas Menzel:** Conceptualization, Data curation, Investigation, Supervision, Writing – review & editing. **Omer Suljevic:** Conceptualization, Resources, Writing – review & editing. **Nicole G. Sommer:** Conceptualization, Resources, Writing – review & editing. **Annelie-M. Weinberg:** Conceptualization, Funding acquisition, Resources, Writing – review & editing. **Christian Appel:** Investigation, Writing – review & editing. **Marianne Liebi:** Supervision, Writing – review & editing. **Ana Diaz:** Investigation, Writing – review & editing. **Lukas Pircher:** Conceptualization, Software, Writing – review & editing. **Christian Hellmich:** Conceptualization, Funding acquisition, Writing – review & editing. **Uwe Y. Schwarze:** Resources, Writing – review & editing. **Helga C. Lichtenegger:** Conceptualization, Data curation, Funding acquisition, Project administration, Supervision, Writing – review & editing. **Tilman A. Grünewald:** Conceptualization, Supervision, Writing – review & editing.

Declaration of competing interest

The authors declare the following financial interests/personal relationships which may be considered as potential competing interests:

Annelie M Weinberg is a shareholder of Bioretec Ltd. All other authors declare that they have no known competing financial interests or personal relationships that could have appeared to influence the work reported in this paper.

Data statement

The data that support the findings of this study are available from the corresponding author, [HL], upon request.

Acknowledgements

This work was supported by the Austrian Science Fund (FWF) (Grant doi 10.55776/I4409) and the Swiss National Science Foundation (SNSF) (Grant number 310030E_188993).

We also acknowledge the Paul Scherrer Institute (PSI) for granting experimental time at the cSAXS beamline of the Swiss Light Source. We thank Oliver Bunk for the fruitful discussions.

TG has received funding from the European Union, European Research Council Horizon Europe, TexTOM (grant no. 101041871). Views and opinions expressed are those of the author(s) only and do not necessarily reflect those of the European Union or the European Research Council. Neither the European Union nor the granting authority can be held responsible for them.

CA has received funding from the European Union's Horizon 2020 research and innovation program under the Marie Skłodowska-Curie grant agreement No 884104 and is also supported by funding from Chalmers initiative for advancement of neutron and X-ray techniques.

Supplementary materials

Supplementary material associated with this article can be found, in the online version, at doi:10.1016/j.actbio.2024.12.008.

References

[1] M.P. Yavropoulou, J. Yovos, The molecular basis of bone mechanotransduction, J. Musculoskelet Neuronal Interact 16 (2016) 221–236.

[2] V.I. Sikavitsas, J.S. Temenoff, A.G. Mikos, Biomaterials and bone mechanotransduction. Biomaterials 22 (19) (2001) 2581–2593, https://doi.org/10.1016/S0142-9612(01)00002-3.

[3] R.L. Duncan, C.H. Turner, Mechanotransduction and the functional response of bone to mechanical strain, Calcif. Tissue Int. 57 (5) (1995) 344–358, https://doi.org/10.1007/BF00302070.

[4] D.F. Williams, Biocompatibility Pathways: biomaterials-Induced Sterile Inflammation, Mechanotransduction, and Principles of Biocompatibility Control, ACS. Biomater. Sci. Eng. 3 (1) (2017) 2–35, https://doi.org/10.1021/acsbiomaterials.6b00607.

[5] L. Geris, et al., Numerical simulation of tissue differentiation around loaded titanium implants in a bone chamber, J. Biomech. 37 (5) (2004) 763–769, https://doi.org/10.1016/j.jbiomech.2003.09.026.

[6] T.H. Huang, et al., Effects of different exercise modes on mineralization, structure, and biomechanical properties of growing bone, J. Appl. Physiol. 95 (1) (2003) 300–307, https://doi.org/10.1152/japplphysiol.01076.2002.

[7] S. Shimomura, et al., Treadmill Running Ameliorates Destruction of Articular Cartilage and Subchondral Bone, Not Only Synovitis, in a Rheumatoid Arthritis Rat Model, Int. J. Mol. Sci. 19 (2018), https://doi.org/10.3390/ijms19061653.

[8] J. Iwamoto, et al., Effects of treadmill exercise on bone mass, bone metabolism, and calciotropic hormones in young growing rats, J. Bone Miner. Metab. 22 (1) (2004) 26–31, https://doi.org/10.1007/s00774-003-0443-5.

[9] C. Bourzac, et al., Preventive Moderate Continuous Running-Exercise Conditioning Improves the Healing of Non-Critical Size Bone Defects in Male Wistar Rats: a Pilot Study Using microCT, Life (Basel) (12) (2020) 10, https://doi.org/10.3390/life10120308.

[10] O. Suljevic, et al., Does early post-operative exercise influence bone healing kinetics? Preclinical evaluation of non-critical sized femur defect healing, Bone 176 (2023) 116869, https://doi.org/10.1016/j.bone.2023.116869.

[11] C. Castellani, et al., Bone-implant interface strength and osseointegration: biodegradable magnesium alloy versus standard titanium control, Acta Biomater. 7 (1) (2011) 432–440, https://doi.org/10.1016/j.actbio.2010.08.020.

[12] F. Witte, et al., In vivo corrosion of four magnesium alloys and the associated bone response, Biomaterials 26 (17) (2005) 3557–3563, https://doi.org/10.1016/j.biomaterials.2004.09.049.

[13] T. Kraus, et al., The influence of biodegradable magnesium implants on the growth plate, Acta Biomater. 66 (2018) 109–117, https://doi.org/10.1016/j.actbio.2017.11.031.

[14] G. Uppal, et al., Magnesium based implants for functional bone tissue regeneration – A review, Journal of Magnesium and Alloys 10 (2) (2022) 356–386, https://doi.org/10.1016/j.jma.2021.08.017.

[15] T.A. Grunewald, et al., Reaction of bone nanostructure to a biodegrading Magnesium WZ21 implant - A scanning small-angle X-ray scattering time study, Acta Biomater. 31 (2016) 448–457, https://doi.org/10.1016/j.actbio.2015.11.049.

[16] T.A. Grunewald, et al., Magnesium from bioresorbable implants: distribution and impact on the nano- and mineral structure of bone, Biomaterials 76 (2016) 250–260, https://doi.org/10.1016/j.biomaterials.2015.10.054.

[17] B. Zeller-Plumhoff, et al., Analysis of the bone ultrastructure around biodegradable Mg-xGd implants using small angle X-ray scattering and X-ray diffraction, Acta Biomater. 101 (2020) 637–645, https://doi.org/10.1016/j.actbio.2019.11.030.

[18] P. Fratzl, R. Weinkamer, Nature's hierarchical materials, Prog. Mater. Sci. 52 (8) (2007) 1263–1334, https://doi.org/10.1016/j.pmatsci.2007.06.001.

[19] C. Hellmich, F.J. Ulm, Are mineralized tissues open crystal foams reinforced by crosslinked collagen?—Some energy arguments, J. Biomech. 35 (9) (2002) 1199–1212, https://doi.org/10.1016/S0021-9290(02)00080-5.

[20] A. Rodriguez-Palomo, M. Østergaard, H. Birkedal, Bone Hierarchical Structure: heterogeneity and Uniformity, Adv. Funct. Mater. (2023), https://doi.org/10.1002/adfm.202307026.

[21] N.K. Wittig, H. Birkedal, Bone hierarchical structure: spatial variation across length scales, Acta Crystallogr. B Struct. Sci. Cryst. Eng. Mater. 78 (2022) 305–311, https://doi.org/10.1107/S2052520622001524. Pt 3 Pt 1.

[22] R.B. Martin, J. Ishida, The relative effects of collagen fiber orientation, porosity, density, and mineralization on bone strength, J. Biomech. 22 (5) (1989) 419–426, https://doi.org/10.1016/0021-9290(89)90202-9.

[23] N. Reznikov, et al., Fractal-like hierarchical organization of bone begins at the nanoscale, Science (1979) 360 (6388) (2018) eaao2189, https://doi.org/10.1126/science.aao2189.

[24] T.A. Grünewald, et al., Mapping the 3D orientation of nanocrystals and nanostructures in human bone: indications of novel structural features, Sci. Adv. 6 (24) (2020) eaba4171, https://doi.org/10.1126/sciadv.aba4171.

[25] T. Tang, et al., A 3D Network of Nanochannels for Possible Ion and Molecule Transit in Mineralizing Bone and Cartilage, Adv. Nanobiomed. Res. 2 (8) (2022), https://doi.org/10.1002/anbr.202100162.

[26] M. Robin, et al., Acidic Osteoid Templates the Plywood Structure of Bone Tissue, Adv. Sci. (Weinh) 11 (9) (2024) e2304454, https://doi.org/10.1002/advs.202304454.

[27] N. Reznikov, et al., Biological stenciling of mineralization in the skeleton: local enzymatic removal of inhibitors in the extracellular matrix, Bone 138 (2020) 115447, https://doi.org/10.1016/j.bone.2020.115447.

[28] Y. Xu, et al., Intermolecular channels direct crystal orientation in mineralized collagen, Nat. Commun. 11 (1) (2020) 5068, https://doi.org/10.1038/s41467-020-18846-2.

[29] P. Fratzl, et al., Nucleation and growth of mineral crystals in bone studied by small-angle X-ray scattering, Calcif. Tissue Int. 48 (6) (1991) 407–413, https://doi.org/10.1007/BF02556454.

[30] F.A. Shah, P. Thomsen, A. Palmquist, Osseointegration and current interpretations of the bone-implant interface, Acta Biomater. 84 (2019) 1–15, https://doi.org/10.1016/j.actbio.2018.11.018.

[31] P. De Falco, et al., Tomographic X-ray scattering based on invariant reconstruction: analysis of the 3D nanostructure of bovine bone, J. Appl. Crystallogr. 54 (Pt 2) (2021) 486–497, https://doi.org/10.1107/S1600576721000881.

[32] M.H. Bunger, et al., Bone nanostructure near titanium and porous tantalum implants studied by scanning small angle x-ray scattering, Eur. Cell Mater. 12 (2006) 81–91, https://doi.org/10.22203/ecm.v012a10.

[33] R.M. Hoerth, et al., A comparative study of zirconium and titanium implants in rat: osseointegration and bone material quality, Journal of Materials Science: Materials in Medicine 25 (2) (2014) 411–422, https://doi.org/10.1007/s10856-013-5074-3.

[34] M. Liebi, et al., Nanostructure surveys of macroscopic specimens by small-angle scattering tensor tomography, Nature 527 (7578) (2015) 349–352, https://doi.org/10.1038/nature16056.

[35] F. Schaff, et al., Six-dimensional real and reciprocal space small-angle X-ray scattering tomography, Nature 527 (7578) (2015) 353–356, https://doi.org/10.1038/nature16060.

[36] M. Liebi, et al., 3D nanoscale analysis of bone healing around degrading Mg implants evaluated by X-ray scattering tensor tomography, Acta Biomater. 134 (2021) 804–817, https://doi.org/10.1016/j.actbio.2021.07.060.

[37] B. Okutan, et al., The combined effect of zinc and calcium on the biodegradation of ultrahigh-purity magnesium implants, Biomater. Adv. 146 (2023) 213287, https://doi.org/10.1016/j.bioadv.2023.213287.

[38] I. Silva Barreto, et al., Micro- and nanostructure specific X-ray tomography reveals less matrix formation and altered collagen organization following reduced loading during Achilles tendon healing, Acta Biomater. 174 (2024) 245–257, https://doi.org/10.1016/j.actbio.2023.12.015.

[39] CXS group, Paul Scherrer Institute, Switzerland, cSAXS matlab package. Available from: https://www.psi.ch/en/sls/csaxs/software.

[40] M. Odstrcil, et al., Alignment methods for nanotomography with deep subpixel accuracy, Opt. Express. 27 (25) (2019) 36637–36652, https://doi.org/10.1364/OE.27.036637.

[41] M. Liebi, et al., Small-angle X-ray scattering tensor tomography: model of the three-dimensional reciprocal-space map, reconstruction algorithm and angular sampling requirements, Acta Crystallogr. a Found. Adv. 74 (Pt 1) (2018) 12–24, https://doi.org/10.1107/S205327331701614X.

[42] P. Fratzl, et al., Diffracting "stacks of cards" - some thoughts about small-angle scattering from bone. Scattering Methods and the Properties of Polymer Materials, N. Stribeck and B. Smarsly, Springer Berlin Heidelberg, Berlin, Heidelberg, 2005, pp. 33–39.

[43] I. Zizak, et al., Characteristics of mineral particles in the human bone/cartilage interface, J. Struct. Biol. 141 (3) (2003) 208–217, https://doi.org/10.1016/S1047-8477(02)00635-4.

[44] S. Rinnerthaler, et al., Scanning Small Angle X-ray Scattering Analysis of Human Bone Sections, Calcif. Tissue Int. 64 (5) (1999) 422–429, https://doi.org/10.1007/PL00005824.

[45] S. Pabisch, et al., Imaging the nanostructure of bone and dentin through small- and wide-angle X-ray scattering, Methods Enzymol. 532 (2013) 391–413, https://doi.org/10.1016/B978-0-12-416617-2.00018-7.

[46] Y. Liu, et al., Size and habit of mineral particles in bone and mineralized callus during bone healing in sheep, J. Bone Miner. Res. 25 (9) (2010) 2029–2038, https://doi.org/10.1002/jbmr.84.

[47] R.M. Hoerth, et al., Correlations between nanostructure and micromechanical properties of healing bone, J. Mech. Behav. Biomed. Mater. 77 (2018) 258–266, https://doi.org/10.1016/j.jmbbm.2017.08.022.

[48] J. Heřt, P. Fiala, M. Petrtýl, Osteon orientation of the diaphysis of the long bones in man, Bone 15 (3) (1994) 269–277, https://doi.org/10.1016/8756-3282(94)90288-7.

[49] F.L. Bach-Gansmo, et al., Calcified cartilage islands in rat cortical bone, Calcif. Tissue Int. 92 (4) (2013) 330–338, https://doi.org/10.1007/s00223-012-9682-6.

[50] A. Shipov, et al., Unremodeled endochondral bone is a major architectural component of the cortical bone of the rat (Rattus norvegicus), J. Struct. Biol. 183 (2) (2013) 132–140, https://doi.org/10.1016/j.jsb.2013.04.010.

[51] P. Roschger, et al., Structural Development of the Mineralized Tissue in the Human L4 Vertebral Body, J. Struct. Biol. 136 (2) (2001) 126–136, https://doi.org/10.1006/jsbi.2001.4427.

[52] R.M. Hoerth, et al., Mechanical and structural properties of bone in non-critical and critical healing in rat, Acta Biomater. 10 (9) (2014) 4009–4019, https://doi.org/10.1016/j.actbio.2014.06.003.

[53] N.K. Wittig, et al., Bone Biomineral Properties Vary across Human Osteonal Bone, ACS. Nano 13 (11) (2019) 12949–12956, https://doi.org/10.1021/acsnano.9b05535.

[54] T.A. Grünewald, et al., Bone mineral properties and 3D orientation of human lamellar bone around cement lines and the Haversian system, IUCrJ. 10 (2023) 189–198, https://doi.org/10.1107/S2052252523000866.

[55] P. Varga, et al., Investigation of the three-dimensional orientation of mineralized collagen fibrils in human lamellar bone using synchrotron X-ray phase nano-tomography, Acta Biomater. 9 (9) (2013) 8118–8127, https://doi.org/10.1016/j.actbio.2013.05.015.

[56] E. Slaets, et al., Early Cellular Responses in Cortical Bone Healing Around Unloaded Titanium Implants: an Animal Study, J. Periodontol. 77 (6) (2006) 1015–1024, https://doi.org/10.1902/jop.2006.050196.

[57] K. Iskhakova, et al., Multi-modal investigation of the bone micro- and ultrastructure, and elemental distribution in the presence of Mg-xGd screws at mid-term healing stages, Bioact. Mater. 41 (2024) 657–671, https://doi.org/10.1016/j.bioactmat.2024.07.019.

[58] C. Lange, et al., Fetal and postnatal mouse bone tissue contains more calcium than is present in hydroxyapatite, J. Struct. Biol. 176 (2) (2011) 159–167, https://doi.org/10.1016/j.jsb.2011.08.003.

[59] A. Cedola, et al., Engineered bone from bone marrow stromal cells: a structural study by an advanced x-ray microdiffraction technique, Phys. Med. Biol. 51 (6) (2006) N109–N116, https://doi.org/10.1088/0031-9155/51/6/N02.

[60] A. Cipitria, et al., Porous scaffold architecture guides tissue formation, J. Bone Mineral Res. 27 (6) (2012) 1275–1288, https://doi.org/10.1002/jbmr.1589.